

Thermal conductivity of various CFRPs from 100 mK to 20 K

Valentin Sauvage^a

^aUniversité Paris Saclay, CNRS, Institut d’Astrophysique Spatiale, Building 121, Orsay, 91400, France

Abstract

Carbon-fiber-reinforced polymers (CFRPs) are among the most promising structural materials for aerospace applications, particularly for systems operating at cryogenic temperatures, where high strength, low mass, and low thermal conductivity are essential. In this work, the thermal conductivity of a set of CFRP samples—T300 (67% 0°), T700 (62% 0°), HS40 (67% 0°/0°/0°/90°), HS40 (62% 0°/0°/0°/90°), M55J (0°), HS40 (67% 0°), HS40 (62% 0°), IMA (0°), and IMA (90°)—was measured over the temperature range 100 mK to 20 K. Thermal conductivities were extracted using a new analysis method developed. The resulting temperature-dependent behavior for each sample is presented and compared with the existing literature.

Keywords: Thermal conductivity, CFRP, carbon fibers, space instrumentation, very low temperature, phonon scattering

1. Introduction

Carbon-fiber-reinforced polymers (CFRPs) are playing an increasingly central role in the development of advanced space structures, owing to their combination of low mass, high stiffness, and excellent dimensional stability under severe environmental constraints. Their use has progressively expanded from conventional aerospace components to the highly demanding domain of cryogenic space instrumentation, where structural elements must simultaneously ensure mechanical integrity and stringent thermal isolation. Recent overviews of composite materials for space applications underline this trend, emphasizing the versatility and growing maturity of high-performance CFRPs in orbital and deep-space environments (Tserpes and Sioutis [2025]). At the same time, several space missions—notably the *Herschel* Space Observatory (McDonald et al. [2006]), the *Planck* Space Observatory (Planck Collaboration [2011]), the Mid-Infrared Instrument (MIRI) (Shaughnessy et al. [2007]) on the *James Webb Space Telescope*—have relied on CFRP struts or support structures precisely because of their reduced thermal conductivity at low temperatures.

However, despite this widespread adoption, the availability of experimental data describing the thermal conductivity of CFRPs at very low temperatures remains limited. Existing measurements typically do not extend below 30–40 K and are often restricted to specific layer configurations or fiber developed for individual missions (Tuttle et al. [2017]). Yet, for modern cryogenic instruments operating between a few kelvin and the millikelvin range, accurate knowledge of the thermal behavior of CFRP components is indispensable. The thermal transport properties depend sensitively on fibre types, volume fractions, and laminate architecture. In this context, the present work aims to provide a characterization of several CFRP materials between 100 mK and 20 K, thereby furnishing the quantitative data required for refined thermal modeling and for the design of structural elements in upcoming low-temperature space mis-

sions.

2. The thermal conductivity

The thermal conductivity κ is a physical quantity characterizing the material’s ability to conduct heat.

Knowing the thermal conductivity of a material allows for the calculation of the power \dot{Q} involved in generating a thermal gradient T_2 to T_1 along a length L through a cross-section S . This relation is given by the equation 1.

$$\dot{Q} = \frac{S}{L} \int_{T_1}^{T_2} \kappa(T) dT \quad (1)$$

\dot{Q} :	the power flowing through the sample	[W]
S :	the sample section	[m ²]
L :	the distance between the two thermometers	[m]
T_1 :	the bottom temperature	[K]
T_2 :	the top temperature	[K]
κ :	the sample thermal conductivity	[W.m ⁻¹ .K ⁻¹]

This equation defines the way the thermal conductivity will be determined using the method presented in section 4.

3. Experimental setup

We developed an experimental setup designed to extract the thermal conductivity consistent with the parameters required in equation 1. This configuration was implemented at the Institut d’Astrophysique Spatiale within the DRACuLA cryostat described in Sauvage [2023]. The system is a BlueFors

LD400 dilution refrigerator capable of reaching temperatures below 10 mK, with a cooling power of 500 μW at 100 mK. The cryostat provides a 290 mm diameter cold plate and an available height of 400 mm, allowing for mounting several samples simultaneously. The radiative environment during the measurements is approximately 1 K.

Figure 1 represents the sample fully instrumented while placed on the cold plate.

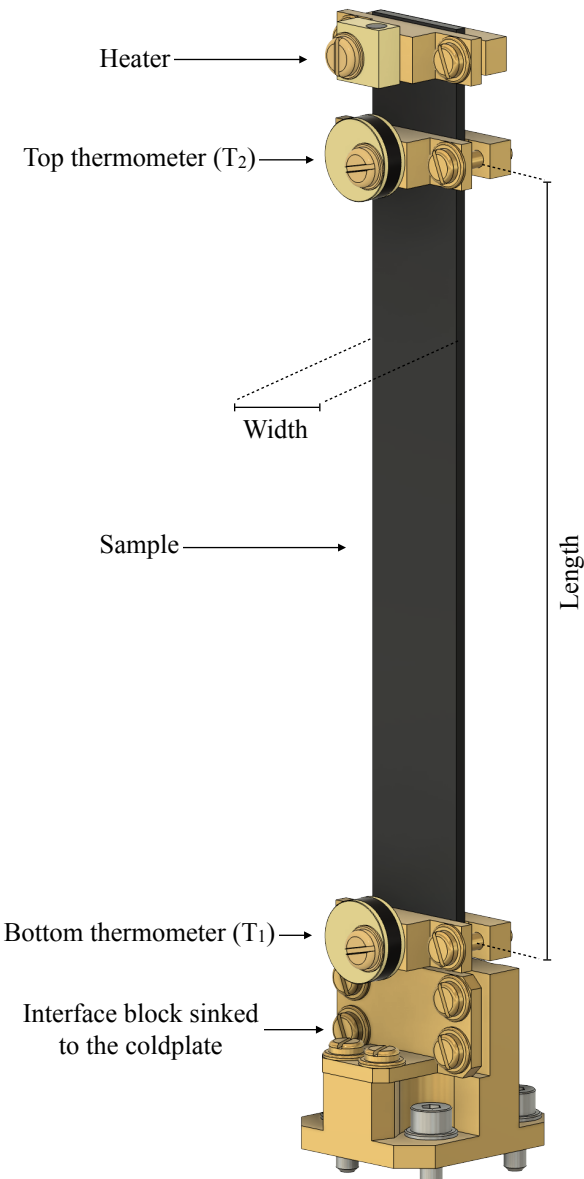


Figure 1: The instrumented sample was placed on the cold plate.

3.1. Thermometry

Two thermometers are used to determine the thermal conductivity of the sample, distant by a length L . One is on top

of the sample and provides T_2 , and one is at the bottom of the sample and provides T_1 . The two thermometers need to be in contact with the sample, a dedicated system has been designed to ensure this contact, as shown in Figure 2. Also, to reduce the uncertainties related to the length between the two thermometers, the contact was chosen to be linear and not surface, as represented in Figure 3. The thermometers are mounted by M3x12 brass screws with a tightening torque of 0.61 N.m.

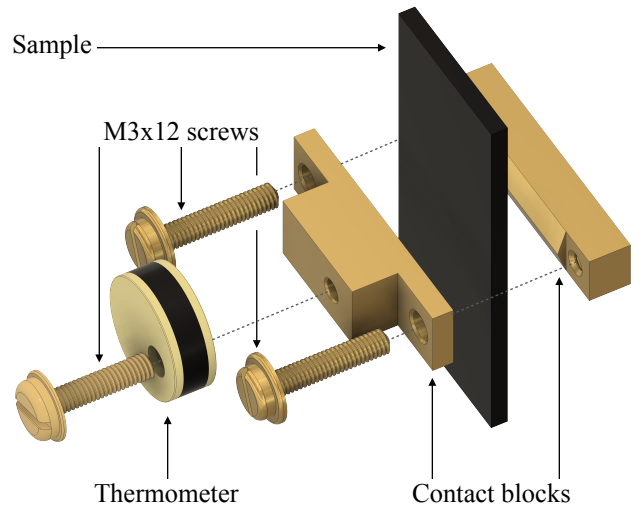


Figure 2: Exploded view of a "linear" contact for both top and bottom thermometers. The choice of a linear contact was made to reduce the uncertainties of the length between the two thermometers.

The bottom thermometer is a Cernox RX-102A (range: [0.05 K-100 K]), and the top thermometer is a Cernox CX-1010 (range: [0.1 K-100 K]). Both are calibrated by the author inside the DRACuLA cryostat ([Sauvage \[2023\]](#)) against the ROx main thermometer of the cryostat. The thermometry is monitored by a Lakeshore 370 AC resistance bridge with an excitation voltage that agrees with the manufacturer's recommendations. The uncertainty of the measured T_1 and T_2 is assumed to be 1%, mainly based on the calibration uncertainties.

Both thermometers are connected by four phosphor-bronze 127 μm wire of 400 mm to the cold-plate cryostat connectors bracket.

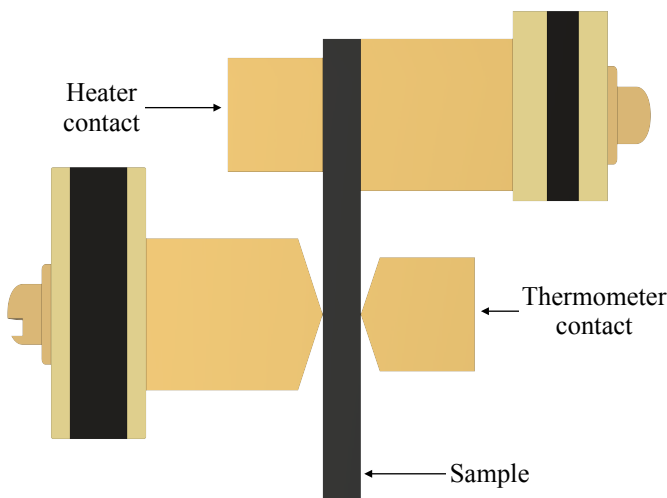


Figure 3: On top the contact for the heater to maximize the injected power into the sample, and on bottom the linear contact for the thermometry to limit the uncertainties of the length between the two thermometers.

3.2. Heater

To generate the thermal gradient along the length, a heater is placed on top of the sample. The heater is composed of a $10\text{ k}\Omega$ thin metallic film resistor (with low $\frac{\Delta R}{\Delta T}$) confined into a gold-plated copper block with Styccast 2850-FT. The heater is thermally connected to the sample by a dedicated design shown in Figure 4, where all M3x12 brass screws were tightened with a torque of 0.61 N.m.

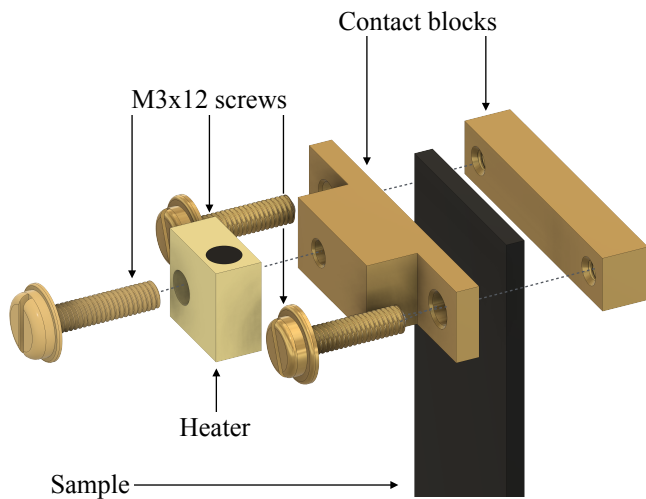


Figure 4: Exploded view of the interface design to thermally couple the heater and the sample.

The heater is connected to the cold-plate cryostat connectors bracket by four phosphor-bronze 127 μm wires of a 400 mm minimum length. A current is injected through the resistance, and the voltage is monitored at both ends, by a Keithley 2602A.

This method provides the true power injected, \dot{Q} , through the sample. The uncertainty of the measured \dot{Q} is assumed to be 0.1% according to the recent instrumental calibration.

3.3. Interface with the cryostat

The sample needs to be anchored on the cold plate for proper thermalization. To do that, the design presented in Figure 5 is used. Four A2-70 M4x12 screws are used to anchor the interface to the cold plate. Both contact surfaces have been cleaned, and a torque of 1.4 N.m was applied. Then, the sample is clamped between the thermalization block and the sample blocker with M3x12 brass screws (torque 0.61 N.m).

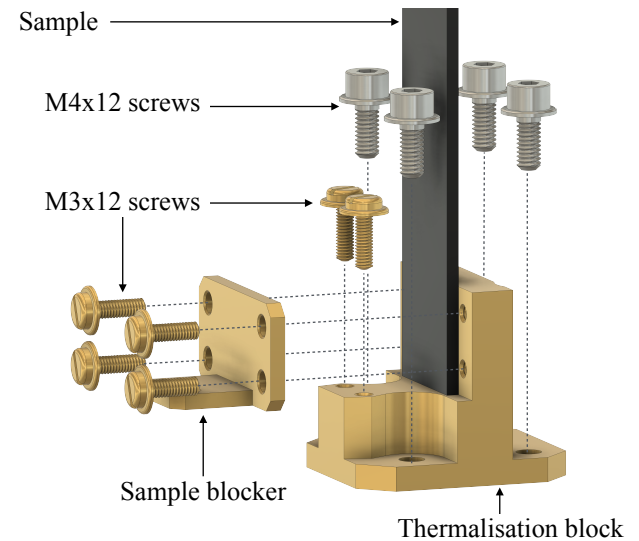


Figure 5: Mechanical design to anchor the sample on the cold plate of the cryostat. To ensure good thermal contact, the interface is a large surface between the sample and the copper gold-plated cold plate.

4. Method

4.1. Determination of T_1 , T_2 and \dot{Q}

In order to determine the thermal conductivity experimentally, a sequence of various powers from nW to mW (defined as "step") is injected at one end of the sample (Figure 6, bottom plot), and the temperature of both thermometers is monitored (Figure 6, top plot). Each step lasted 3 hours.

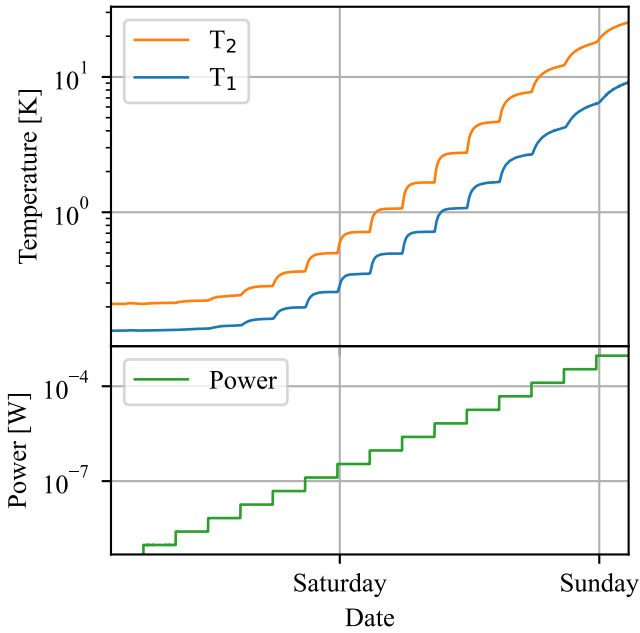


Figure 6: Top plot showing the temperature evolution of the two thermometers and the injected power on bottom plot against the time.

From the raw data, the temperature and the time constant are extracted. Each step is fitted with equation 2.

$$T(t) = A - Be^{-\frac{t}{\tau}} \quad (2)$$

T :	the temperature against time	[K]
A :	a parameter	[K]
B :	a parameter	[K]
t :	the time	[s]
τ :	the time constant	[s]

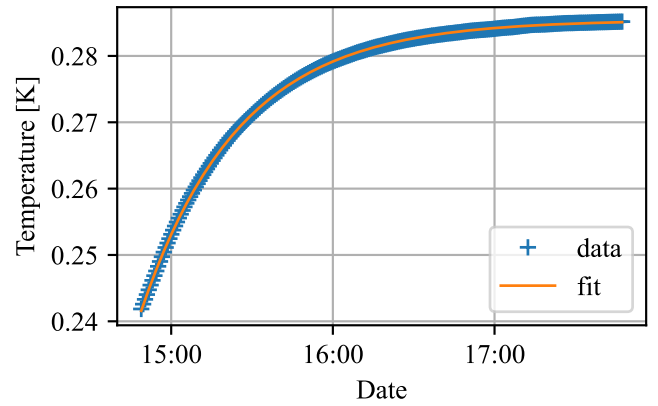


Figure 7: Example of the fit of one step using equation 2. The data are represented together with the fit.

The average of the measured power is designated as \dot{Q} , while its standard deviation over the duration of the step is considered as the associated uncertainty. The fitting method is applied for each steps, and the results are shown in Figure 8, where T_1 and T_2 are represented against the injected power, together with their measurement and fit uncertainties.

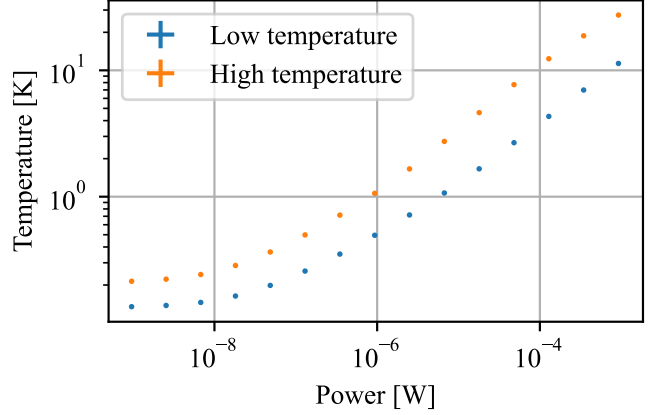


Figure 8: Graphical representation of both temperature measurements against the injected power, together with their uncertainties.

The parameter B , the final temperature reached at equilibrium, can be from equation 2. Hence, there is no need to wait for the temperature stabilization of the system. In return, an uncertainty is associated with the final temperature and is taken into account for the rest of this paper. Figure 7 shows an example of a step together with its associated fit. This method provides T_1 and T_2 .

We can also provide the time constant for every measured steps, represented in Figure 9. The time constant value reach a minimum around $1 \mu\text{W}$, which corresponds to approximately 1 K, which is due to a trade off between the thermal conductivity and the specific heat. Note that the specific heat will not be determined in this paper.

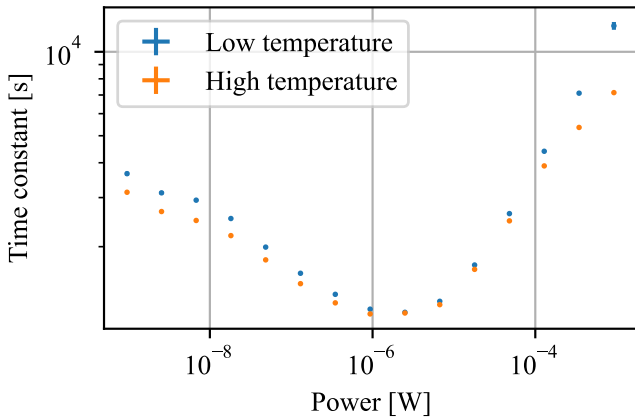


Figure 9: Graphical representation of the time constant for both thermometers against the injected power, together with their uncertainties.

For each fit, the goodness of fit is assessed using the χ^2 method, with the results shown in Figure 10. This evaluation provides a measure of how well the model corresponds to the data. The lower χ^2 value, the better the fit is. Given the number of data points measured for each step, a χ^2 value below 10 is deemed excellent.

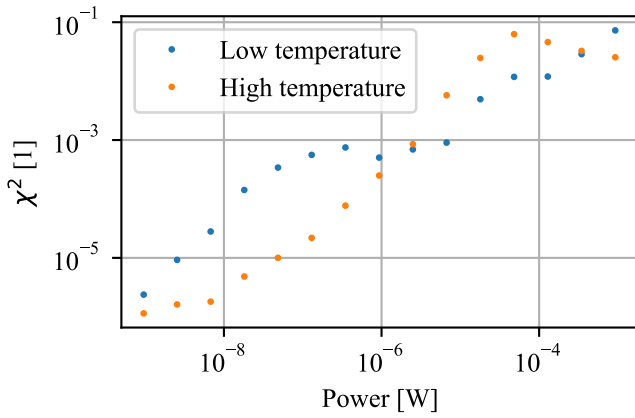


Figure 10: Graphical representation of the χ^2 for every fit performed (lower is better).

4.2. Determination of \dot{Q}_0

Since equation 1 is theoretical and does not account for the environmental setup, it is incomplete. To address this, a parameter, \dot{Q}_0 , must be introduced. This parameter represents an additional heating originating from the environment, which generates a constant thermal gradient. The influence of \dot{Q}_0 becomes significant when the injected power \dot{Q} is low (below 100 nW) and must be subtracted from the data to accurately determine the true \dot{Q} flowing through the sample. Equation 3 is considered to give the thermal conductivity of the sample.

$$\dot{Q} = \frac{S}{L} \int_{T_1}^{T_2} \kappa(T) dT + \dot{Q}_0 \quad (3)$$

4.3. Determination of the thermal conductivity

Then, an algorithm is applied to determine the thermal conductivity, using the `optimize.curve_fit` function from the `scipy` python package. The likelihood of the thermal conductivity $\kappa(T)$ must be provided. To match the thermal conductivity, we adopt a Callaway-type phenomenological equation 4 that express the phonon scattering process, which dominates at low temperatures (Callaway [1959]).

$$\kappa(T) = \frac{aT^3}{1 + bT^n} \quad (4)$$

κ	:	the thermal conductivity	$[\text{W} \cdot \text{m}^{-1} \cdot \text{K}^{-1}]$
T	:	the temperature	[K]
a, b, n	:	fitting parameters	[-]

This model does not include the radiative power loss associated with the emissivity of the sample, which scales as T^4 and becomes relevant whenever the surrounding radiative environment (i.e. the shield temperature) is colder than the sample itself. At higher temperatures, the associated emissive loss may become non-negligible compared to the applied heating power, and the model must therefore be extended accordingly. To quantify this contribution, the radiative power was calculated for emissivity values between 0.01 and 0.2 and compared to the injected power \dot{Q} , as shown in Figure 11. Even in the most conservative case ($\epsilon = 0.2$), the radiative contribution remains below 1%. Its influence is thus neglected.

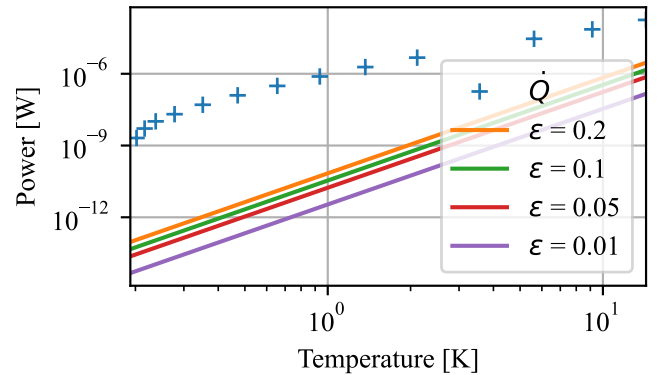


Figure 11: Comparison between the injected power \dot{Q} and the radiative power loss predicted by the model, evaluated for different surface emissivities and temperatures.

Since the injected power covers several orders of magnitude (from 10^{-9} to 10^{-3} W), the convergence criterion of the `optimize.curve_fit` routine, namely the least-square tolerance set at 10^{-6} , is not appropriate for such small fitted values. The fit must therefore be performed in logarithmic space. In order to compute the residuals, the error estimation has also been determined so that the relative weight of the error remains identical, independently of the power, as expressed in equation 5.

$$\text{error} = \sqrt{\frac{1}{N} \sum_{i=1}^N \log\left(\frac{\dot{Q}_i^{\text{fit}}}{\dot{Q}_i^{\text{meas}} + \dot{Q}_0}\right)^2} \quad (5)$$

\dot{Q}^{fit}	: the power fitted with κ	[W]
\dot{Q}^{meas}	: the power injected on sample	[W]
\dot{Q}_0	: the parasitic heat	[W]
N	: the number of measurements	[1]

4.4. Source of uncertainties

This experimental determination method involves several sources of uncertainty, each associated with its respective parameter.

An uncertainty of 0.1% is associated with \dot{Q} , coming from the power measurement. Uncertainties of 1% are associated with T_1 and T_2 , due to thermometer calibration and electronic read-out.

Uncertainties of 0.1% are associated with L and S , resulting from dimensional measurements (measurements available in table 2). The thermal contraction of the sample induces measurable changes in its geometrical dimensions. Because of the preferential fibre orientation, the CFRP exhibits pronounced anisotropy (Sápi and Butler [2020]), which renders the determination of an effective Coefficient of Thermal Expansion (CTE) for the composite particularly challenging. At cryogenic temperatures, the CTE of carbon fibres is known to be very small (Srisuriyachot et al. [2025]), whereas that of the epoxy matrix binding the fibres may reach 2 to 3% (Nakane [2002]). Following the recommendations of previous studies, a uniform correction of 3% has therefore been applied to all geometrical dimensions. In addition, Baschek and Hartwig [1998] reported a variation of approximately 20% in the CTE of samples subjected to thermal cycling, that is not consider in this study.

The power dissipated through the wires was evaluated and found to be consistently negligible compared with the injected power \dot{Q} . The uncertainty associated with radiative losses has already been addressed previously.

All these uncertainties were propagated using a Monte Carlo approach with 200 iterations. They were fully incorporated into the fitting procedure so as to obtain the most reliable estimate of the thermal conductivity together with its overall uncertainty. The residuals between the fitted curve and the experimental data define the final error associated with the method (equation 5). The resulting thermal conductivities are shown in Figure 12, and the corresponding fitting parameters are reported in table 3.

5. Results

Owing to their expected low thermal conductivity and specific heat, the samples required more than three days to

reach thermal equilibrium at the lowest attainable temperature. The samples were mounted in groups of three on the cold plate, but tested individually in order to avoid any mutual parasitic radiative load.

We tested nine commercially available CFRP samples, differing in fiber type, resin content (volume ratio between resin and total volume), and fiber orientation, which are summarized in Table 1. The fiber orientation refers to the angle between the fiber direction and the heat flux: a fiber aligned with the flux is denoted 0° , whereas a transverse fiber is noted 90° .

The CFRP samples were provided into elongated rectangular plates approximately 200 mm in length, 20 mm in width, and 2 mm in thickness. Precise measurements of the geometrical dimensions used in the thermal-conductivity analysis, together with their absolute uncertainties, are given in Table 2.

Sample	Fiber	Fiber content	Angle [°]	Supplier
1	T700	62%	0	NTPT
2	HS40	67%	0/0/0/90	NTPT
3	HS40	62%	0/0/0/90	NTPT
4	M55J	60%	0	Mecano ID
5	HS40	67%	0	NTPT
6	HS40	62%	0	NTPT
7	T300	67%	0	NTPT
8	IMA	60%	90	Mecano ID
9	IMA	60%	0	Mecano ID

Table 1: Details of the CFRP samples tested are presented. The commercial designation, fiber content, fiber-orientation angle, and supplier are provided.

Sample	Length [mm]	Width [mm]	Thickness [mm]
1	144.3 ± 0.1	20.16 ± 0.01	1.97 ± 0.02
2	143.5 ± 0.1	20.16 ± 0.01	1.97 ± 0.02
3	143.5 ± 0.1	20.16 ± 0.01	1.97 ± 0.02
4	55.3 ± 0.1	20.85 ± 0.01	1.97 ± 0.02
5	155.5 ± 0.1	20.16 ± 0.01	1.97 ± 0.02
6	156.2 ± 0.1	20.16 ± 0.01	1.97 ± 0.02
7	156.1 ± 0.1	20.16 ± 0.01	1.97 ± 0.02
8	65.8 ± 0.1	20.16 ± 0.01	1.97 ± 0.02
9	65.5 ± 0.1	20.16 ± 0.01	1.97 ± 0.02

Table 2: CFRP sample geometric dimensions

Applying the method described in section 4, we report the fitting parameters of the thermal conductivity model given in equation 1, together with their relative uncertainties and the corresponding temperature ranges. The resulting thermal conductivities are shown in Figure 12.

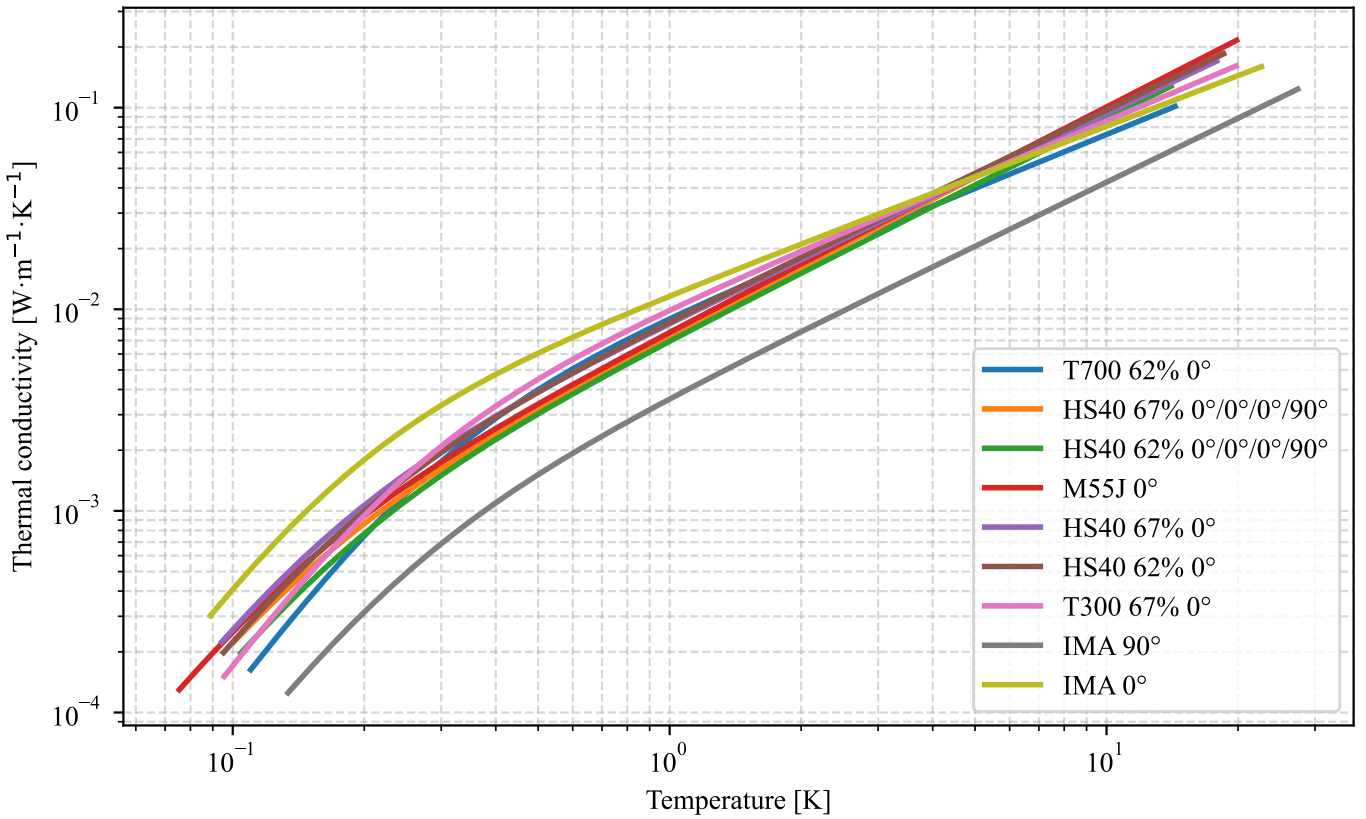


Figure 12: Thermal conductivity of the nine samples that has been determined at IAS over the range of temperature [100 mK - 20 K]

6. Comparison with literature

Unfortunately, although a substantial number of thermal-conductivity measurements can be found in the literature, the corresponding results are often reported simply under generic labels such as “CFRP” or “carbon-fibre composite”, without specifying the fibre type, the epoxy system, or the volume fraction.

In the following, we compare our measurements with the most appropriate data available in the literature. However, no published thermal-conductivity data exist for CFRPs based on HS40 or IMA fibres, which prevents any meaningful comparison for these specific materials. The thermal conductivities are presented in Figure 13 for the HS40 material and in Figure 14 for a more detailed comparison.

6.1. T700

The present 0° measurements exhibit excellent agreement with the data of Amm *et al.* [2000] over the full overlapping temperature interval [5-15 K], both in absolute magnitude and in their temperature dependence, as shown in Figure 15. Conversely, the values reported by Wei *et al.* [2015] are systematically higher: typically by a factor of 1.5–2 for the 0° orientation and by several tens of percent for the 90° direction. This persistent discrepancy, observed in both the fibre-parallel and transverse configurations, likely reflects differences in material formulation, lay-up, fibre volume fraction, or possibly in the experimental protocol itself. In view of the strong consistency between our results and those of Amm *et al.*, and the pronounced

divergence affecting the dataset of Wei *et al.*, it seems that certain aspects of the latter measurements or of their material description remain insufficiently documented. This point should therefore be considered with caution when drawing comparisons.

6.2. T300

The present 0° measurements exhibit good agreement with the 0° data reported by Hartwig and Knaak [1984], as represented in Figure 16. The literature plots for 45° , 90° , and cross-plied laminates follow the expected hierarchy imposed by fibre orientation, with heat transport remaining most efficient along the fibre direction. In contrast, the values published by Bansemir and Haider [1991] are consistently lower than those of Hartwig *et al.* for comparable orientations, which likely reflects differences in material formulation or experimental procedures. These discrepancies should be borne in mind when comparing the various datasets.

6.3. M55J

The present 0° measurements reproduce the overall behaviour reported by Canavan [2006], with comparable values above a few kelvin, as shown in Figure 17. As expected, the fibre-parallel (0°) data of Canavan [2006] remain systematically higher than their 90° measurements, illustrating the pronounced anisotropy of unidirectional CFRP. The slight offset observed between our 0° curve and the corresponding literature values is

consistent with differences in fibre volume fraction, resin system, or laminate architecture, all of which exert a direct influence on the absolute level of thermal conductivity. Overall, both datasets exhibit a similar temperature dependence over the common interval, while the variations in magnitude can be readily attributed to differences in material composition and lay-up.

7. Conclusion

We measured the thermal conductivity of nine CFRP samples with different fiber types, fiber volume fractions, and laminate structures, over temperatures from 100 mK to 20 K. The experimental setup and method developed for this work allow us to obtain reliable values down to the millikelvin range. The data show clear trends linked to fiber orientation and fiber content, and all samples follow the expected low-temperature phonon-scattering behavior.

Compared with the most relevant published results, our measurements agree well with datasets based on similar material definitions. The systematic differences seen in other studies emphasize how important it is to specify composite constituents and processing conditions accurately. The thermal-conductivity parametrization obtained here therefore offers a solid basis for modeling CFRP components in current and future cryogenic space instruments, especially at temperatures where no measurements previously existed.

Our results also show that, for all samples, an inflection in the conductivity curve below 1 K makes extrapolation from higher temperatures unreliable. As a consequence, when CFRPs are used in critical systems operating at sub-Kelvin temperatures, each new material must be characterized. Thermal conductivity must be considered together with mechanical properties to select a suitable CFRP for the intended application.

Acknowledgements

The author would like to thank the CEA—DSBT (Département des Systèmes Basses Températures, Grenoble, France), the IRAP (Institut de Recherche en Astrophysique et Planétologie, Toulouse, France), and MECANO ID (Toulouse, France)

for providing the samples. The author also wish to thank Thomas Prouvé, Jean-Christophe Le Clec'h and Antoine Arondel for their valuable assistance.

References

Amm, K.M., Ackermann, R.A., Thompson, P.S., Mogro-Campero, A., van Oort, J.M., 2000. Thermal conductivity of 34-700 carbon fiber composites at cryogenic temperatures, in: Balachandran, U.B., Hartwig, K.T., Gubser, D.U., Bardos, V.A. (Eds.), *Advances in Cryogenic Engineering Materials: Volume 46, Part A*. Springer US, pp. 313–320. doi:[10.1007/978-1-4615-4293-3_40](https://doi.org/10.1007/978-1-4615-4293-3_40).

Bansemir, H., Haider, O., 1991. Basic material data and structural analysis of fibre composite components for space application 31, 298–306. doi:[10.1016/0011-2275\(91\)90097-G](https://doi.org/10.1016/0011-2275(91)90097-G).

Baschek, G., Hartwig, G., 1998. Parameters influencing the thermal expansion of polymers and fibre composites 38, 99–103. doi:[10.1016/S0011-2275\(97\)00117-3](https://doi.org/10.1016/S0011-2275(97)00117-3).

Callaway, J., 1959. Model for lattice thermal conductivity at low temperatures 113, 1046–1051. doi:[10.1103/PhysRev.113.1046](https://doi.org/10.1103/PhysRev.113.1046).

Canavan, E.R., 2006. Thermal conductivity and specific heat measurements of candidate structural materials for the JWST optical bench, in: AIP Conference Proceedings, AIP. pp. 233–240. doi:[10.1063/1.2192356](https://doi.org/10.1063/1.2192356). ISSN: 0094243X.

Hartwig, G., Knaak, S., 1984. Fibre-epoxy composites at low temperatures 24, 639–647. doi:[10.1016/0011-2275\(84\)90083-3](https://doi.org/10.1016/0011-2275(84)90083-3).

McDonald, P.C., Jaramillo, E., Baudouy, B., 2006. Thermal design of the CFRP support struts for the spatial framework of the herschel space observatory 46, 298–304. doi:[10.1016/j.cryogenics.2005.12.001](https://doi.org/10.1016/j.cryogenics.2005.12.001).

Nakane, H., 2002. Thermal properties of epoxy resins at cryogenic temperatures, in: AIP Conference Proceedings, AIP. pp. 211–220. doi:[10.1063/1.1472545](https://doi.org/10.1063/1.1472545). ISSN: 0094243X.

Table 3: Fitted thermal conductivity parameters for all samples. Values are mean \pm standard deviation from Monte Carlo resampling. Errors are relative RMS values expressed in percent.

Sample	<i>a</i>	<i>b</i>	<i>n</i>	Error [%]	Temperature range [K]
T700 38% 0°	0.140 ± 0.003	14.580 ± 0.474	2.114 ± 0.016	2.44	[0.110 - 14.347]
HS40 33% 0°/0°/0°/90°	0.364 ± 0.028	48.723 ± 4.591	1.880 ± 0.013	4.09	[0.100 - 18.206]
HS40 38% 0°/0°/0°/90°	0.258 ± 0.039	36.157 ± 6.791	1.908 ± 0.032	2.19	[0.104 - 14.044]
M55J 0°	0.427 ± 0.017	54.647 ± 2.879	1.890 ± 0.011	4.43	[0.075 - 19.842]
HS40 33% 0°	0.378 ± 0.014	43.617 ± 2.132	1.967 ± 0.012	3.15	[0.094 - 17.873]
HS40 38% 0°	0.309 ± 0.021	34.897 ± 3.203	1.960 ± 0.018	3.21	[0.095 - 18.531]
T300 33% 0°	0.198 ± 0.006	19.017 ± 0.967	2.082 ± 0.016	3.01	[0.096 - 19.799]
IMA 90°	0.072 ± 0.007	19.108 ± 2.606	1.946 ± 0.023	5.03	[0.134 - 27.387]
IMA 0°	0.533 ± 0.012	44.921 ± 1.698	2.166 ± 0.015	4.85	[0.089 - 22.620]

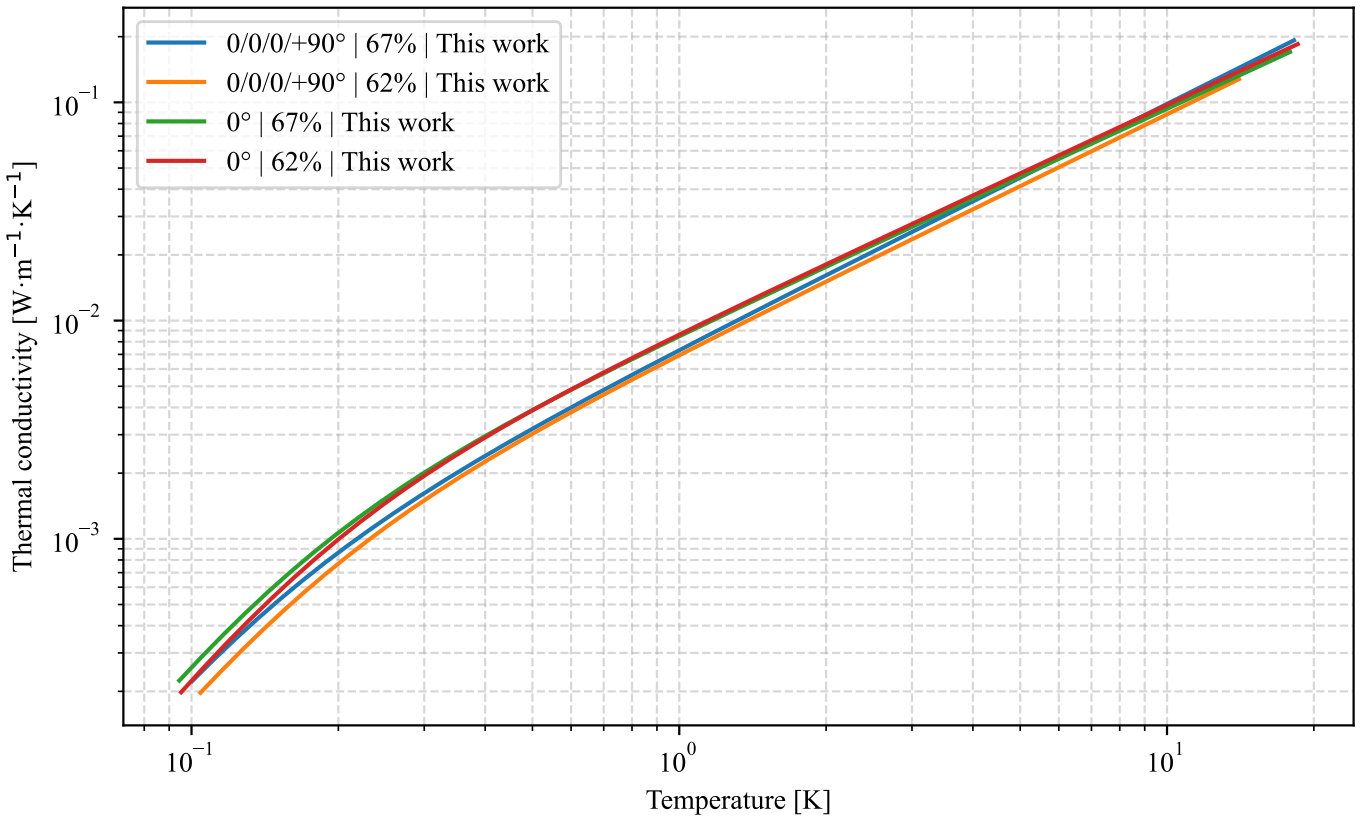


Figure 13: Thermal conductivities for the HS40 samples obtained in this work.

Planck Collaboration, 2011. *Planck* early results. II. the thermal performance of *Planck* 536, A2. doi:[10.1051/0004-6361/201116486](https://doi.org/10.1051/0004-6361/201116486).

Sauvage, V., 2023. Development of a closed-cycle dilution refrigerator for future cosmological missions.

Shaughnessy, B.M., Eccleston, P., Fereday, K.J., Canfer, S.J., Nørgaard-Nielsen, H.U., Jessen, N.C., 2007. Thermal conductivity measurement below 40k of the CFRP tubes for the mid-infrared instrument mounting struts 47, 348–352. doi:[10.1016/j.cryogenics.2007.03.006](https://doi.org/10.1016/j.cryogenics.2007.03.006).

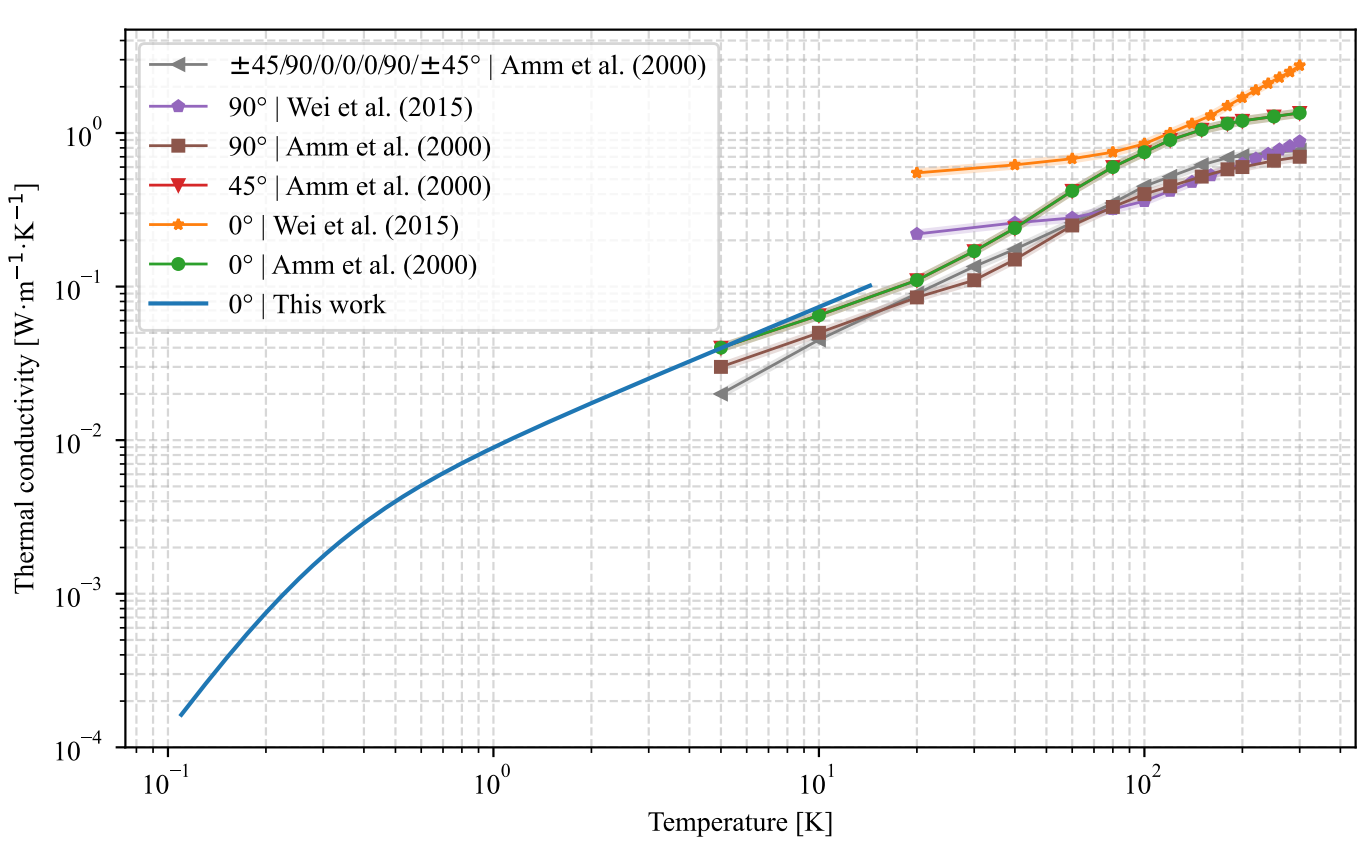
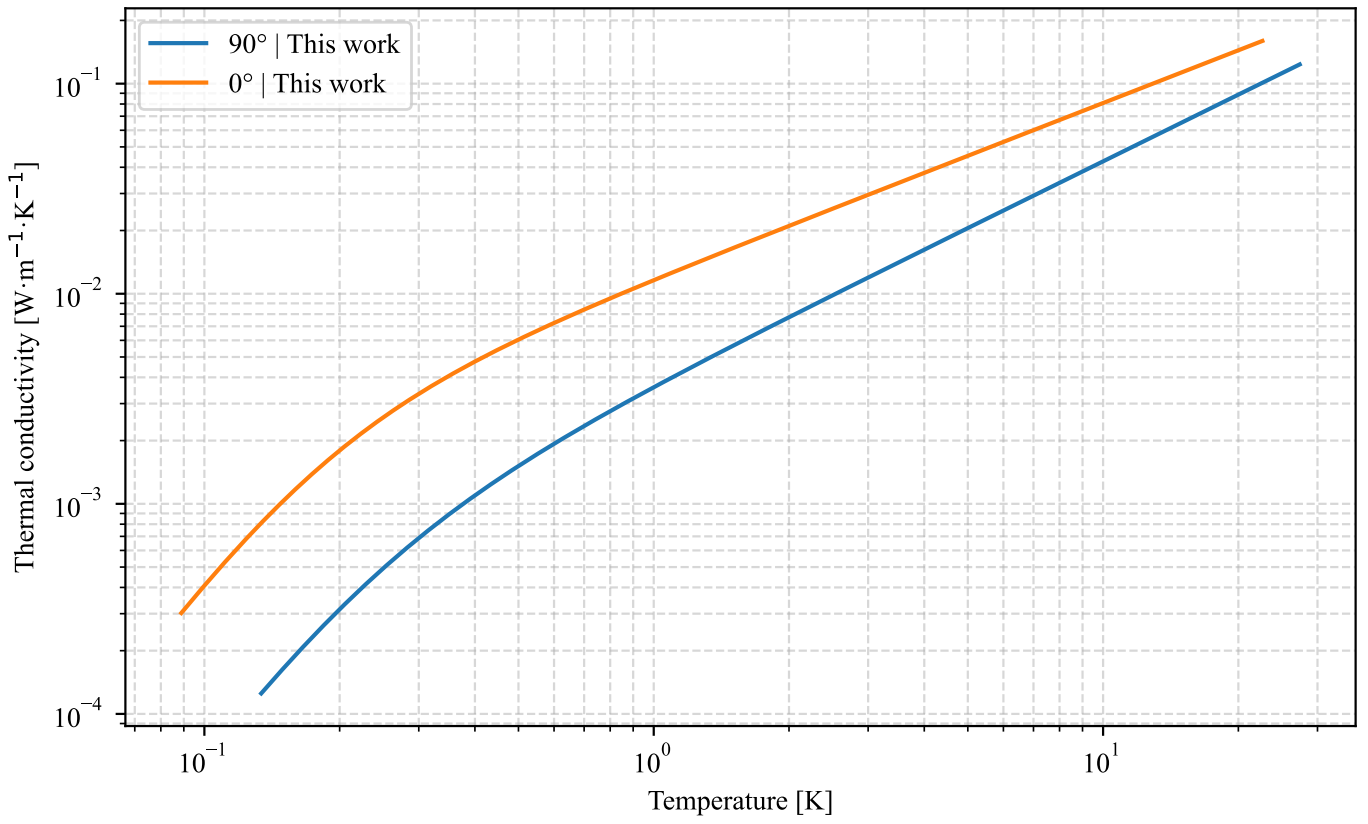
Srisuriyachot, J., Singhapong, W., Rodriguez Santana, P., Sangan, C.M., Bowen, C., Dolbnya, I.P., Butler, R., Lunt, A.J., 2025. Quantification of the thermal expansion of carbon fibres in CFRP at low temperatures using x-ray diffraction 305, 112697. doi:[10.1016/j.compositesb.2025.112697](https://doi.org/10.1016/j.compositesb.2025.112697).

Sápi, Z., Butler, R., 2020. Properties of cryogenic and low temperature composite materials – a review 111, 103190. doi:[10.1016/j.cryogenics.2020.103190](https://doi.org/10.1016/j.cryogenics.2020.103190).

Tserpes, K., Sioutis, I., 2025. Advances in composite materials for space applications: A comprehensive literature review 12, 215. doi:[10.3390/aerospace12030215](https://doi.org/10.3390/aerospace12030215).

Tuttle, J., Canavan, E., Jahromi, A., 2017. Cryogenic thermal conductivity measurements on candidate materials for space missions 88, 36–43. doi:[10.1016/j.cryogenics.2017.10.010](https://doi.org/10.1016/j.cryogenics.2017.10.010).

Wei, W., Rongjin, H., Chuanjun, H., Zhao, Y., Li, S., Laifeng, L., 2015. Cryogenic performances of t700 and t800 carbon fibre- epoxy laminates 102, 012016. doi:[10.1088/1757-899X/102/1/012016](https://doi.org/10.1088/1757-899X/102/1/012016).



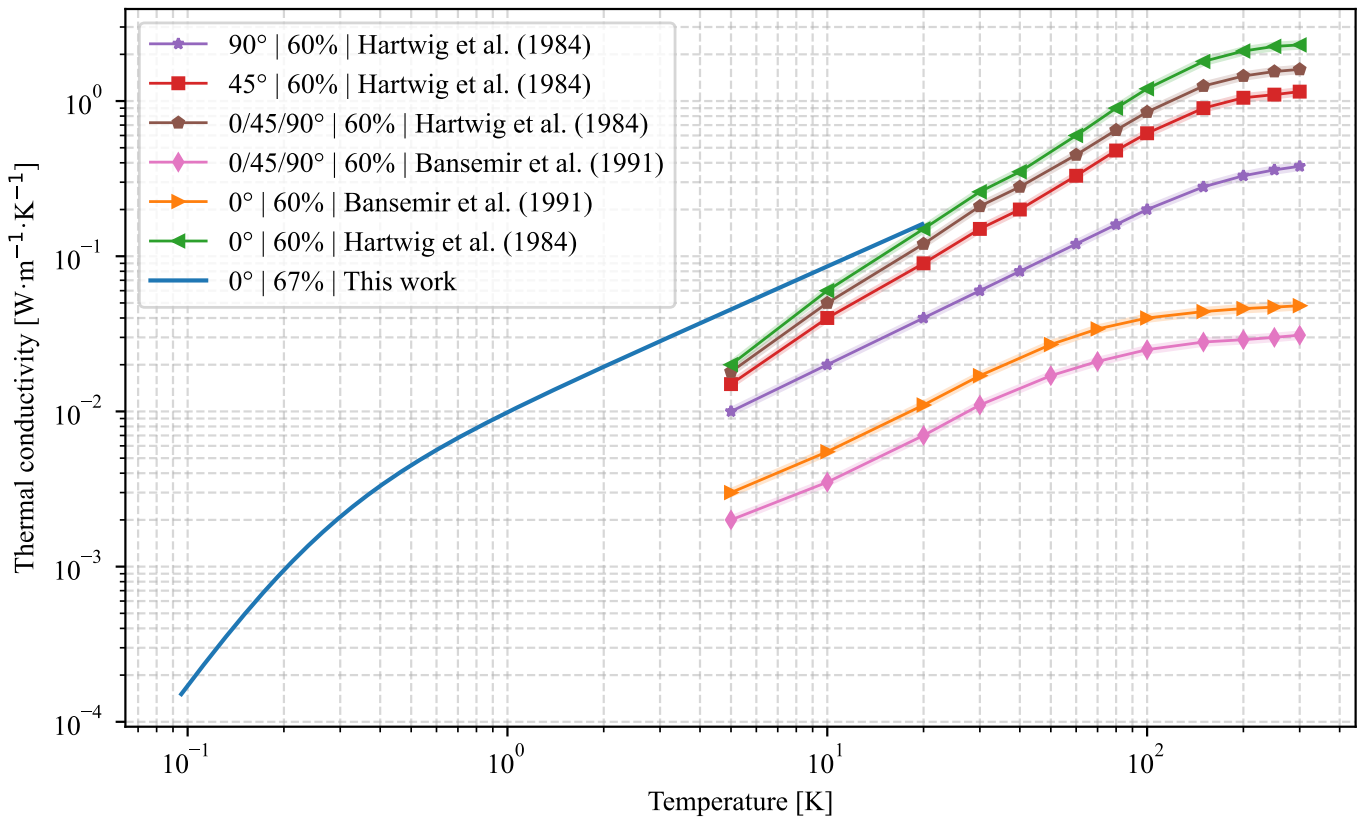


Figure 16: Comparison between the thermal conductivities for T300 obtained in this work and those reported in the literature over the entire temperature range, from room temperature down to the lowest temperatures.

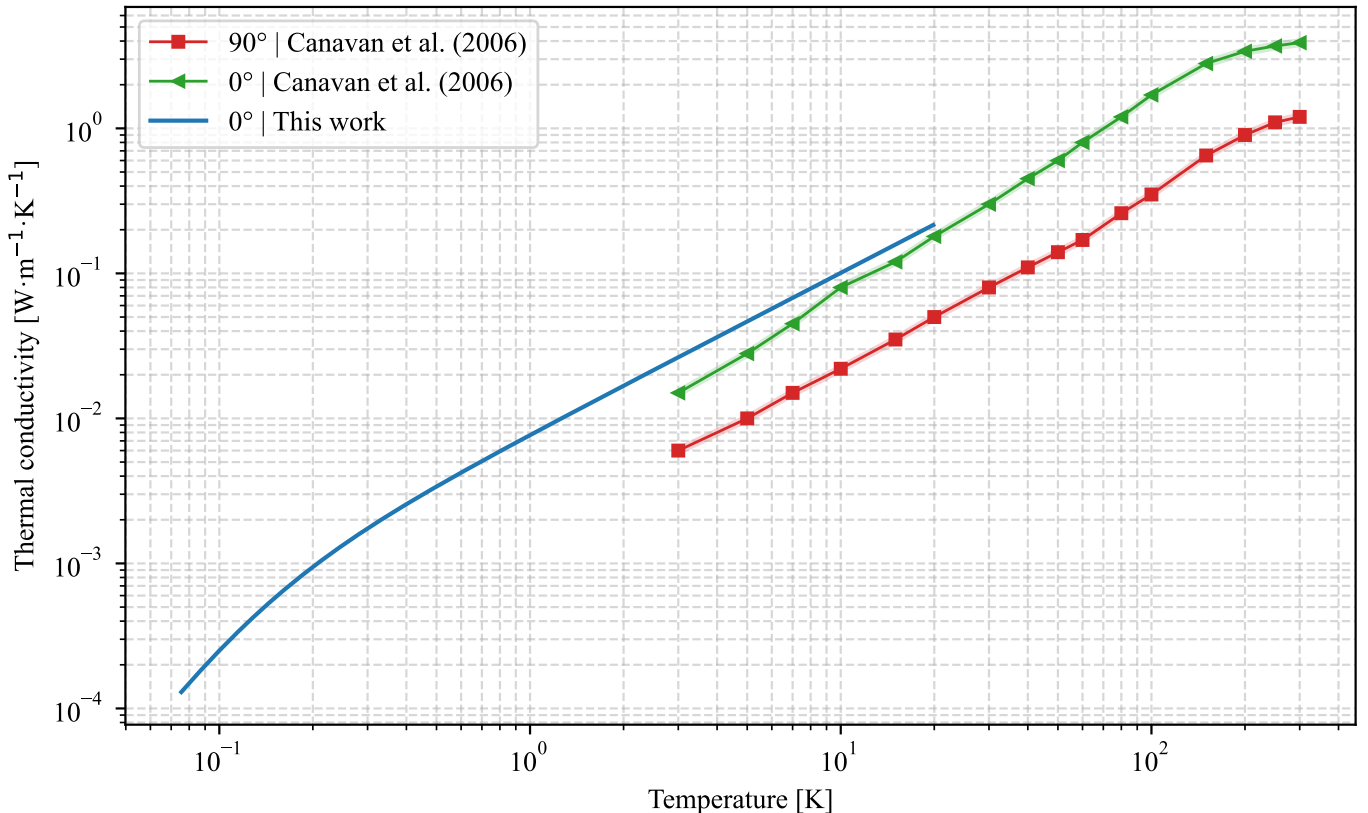


Figure 17: Comparison between the thermal conductivities for M55J obtained in this work and those reported in the literature over the entire temperature range, from room temperature down to the lowest temperatures.